Applied Surface Science 690 (2025) 162618

Contents lists available at ScienceDirect

Applied Surface Science

journal homepage: www.elsevier.com/locate/apsusc

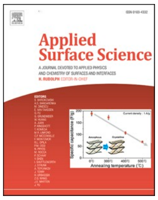

Full Length Article

Fast-responding ethanol sensor with extremely low detection limit: Influence of Pt film thickness on gas sensing properties

Jae Han Chung [a,1], Eunsol Lee [a,1], Junho Hwang [b], Junha Park [c], Seungjong Hwang [a], Dongwook Youm [a], Dohyeon Shin [a], Ki Chang Kwon [d], Soonmin Yim [e], Wooyoung Lee [b], Donghwi Cho [e,f,*], Kwangjae Lee [g,*], Young-Seok Shim [a,*]

[a] School of Energy, Materials and Chemical Engineering, Korea University of Technology and Education (KOREATECH), Cheonan 31253, Republic of Korea
[b] Department of Materials Science and Engineering, Yonsei University, Seoul 03722, Republic of Korea
[c] School of Mechanical Engineering, Korea University of Technology and Education (KOREATECH), Cheonan 31253, Republic of Korea
[d] Interdisciplinary Materials Measurement Institute, Korea Research Institute of Standards and Science (KRISS), Daejeon 34133, Republic of Korea
[e] Thin Film Materials Research Center, Korea Research Institute of Chemical Technology (KRICT), Daejeon 34114, Republic of Korea
[f] Advanced Materials and Chemical Engineering, University of Science and Technology, Daejeon 34113, Republic of Korea
[g] Department of Information Security Engineering, Sangmyung University, Cheonan 31066, Republic of Korea

ARTICLE INFO

Keywords:
In_2O_3
Pt
Nanostructure
Catalysts
Gas sensor

ABSTRACT

To facilitate alcohol detection in exhaled breath, high-performance gas sensors capable of rapidly responding to low-concentration target gases in highly humid environments are required. In this study, we developed In_2O_3 nanorods (NRs) decorated with Pt nanoparticles (NPs) to improve selective C_2H_5OH detection under dry and 80 % relative humidity (RH) conditions. Using glancing angle deposition (GLAD), we fabricated In_2O_3 NRs with Pt film of varying film thicknesses (0.5, 1, and 2 nm), which transformed to NPs after the subsequent annealing process, to systematically identify the optimal Pt NPs size and distribution. Optimized In_2O_3 NRs with an initial Pt thickness of 1 nm exhibited the highest ethanol response at 450 °C, with a theoretical detection limit (DL) calculated to be 0.42 parts per billion (ppb) in dry air and 6.1 ppb under 80 % RH. This enhanced performance is attributed to the expansion of the electron depletion layer (EDL) due to Schottky barrier formation at the Pt-In_2O_3 interface, alongside a spillover effect that enhances gas adsorption and reaction on the In_2O_3 surface, where Pt NPs contribute both electronic and chemical sensitization effects. These findings indicate that In_2O_3 NRs with Pt NPs are promising candidates for next-generation ignition interlock devices (IIDs), offering high selectivity, rapid response times, and stability in high-humidity environments.

1. Introduction

The National Highway Traffic Safety Administration (NHTSA) reports that approximately 10,000 people die each year in the U.S. due to drunk driving-related crashes, accounting for 29 % of all traffic fatalities. There has been a notable increase in these numbers since 2014, indicating a decline in the effectiveness of traditional prevention methods [1]. Law enforcement agencies have intensified efforts to combat drunk driving through stricter enforcement of driving under the influence (DUI) laws, including sobriety checkpoints and harsher penalties. However, studies suggest that while these measures have led to temporary reductions in drunk driving-related fatalities, their long-term effectiveness remains limited [2]. The implementation of IIDs, which require drivers to pass a breathalyzer test before starting their vehicle, has shown promising results in significantly reducing repeat offenses and fatalities [3]. Despite this success, widespread implementation has been challenging due to high costs and logistical issues, such as installation expenses and the relatively large size of the devices [4]. Therefore, various types of gas sensors, such as electrochemical, optical, catalytic combustion-type, and chemoresistive-type have been

---

* Corresponding authors at: Thin Film Materials Research Center, Korea Research Institute of Chemical Technology (KRICT), Daejeon 34114, Republic of Korea (D. Cho); Department of Information Security Engineering, Sangmyung University, Cheonan 31066, Republic of Korea (Kwangjae Lee); School of Energy, Materials and Chemical Engineering, Korea University of Technology and Education (KOREATECH), Cheonan 31253, Republic of Korea (Young-Seok Shim).

E-mail addresses: roy.cho@krict.re.kr (D. Cho), begleam@smu.ac.kr (K. Lee), ysshim@koreatech.ac.kr (Y.-S. Shim).

[1] These authors contributed equally to this work: J.H. Chung, and E. Lee.

https://doi.org/10.1016/j.apsusc.2025.162618
Received 14 November 2024; Received in revised form 30 January 2025; Accepted 2 February 2025

being investigated for the integration into vehicles with high performance and low cost [5–7].

Metal-oxide–semiconductor (MOS)-based gas sensors offer cost-effective, easy integration, and potential for miniaturization, making them promising candidates for integration into the IIDs systems [8]. Among various MOS (SnO_2, ZnO, CuO, and NiO), indium oxide (In_2O_3) has attracted significant attention due to its wide bandgap (3.5–3.7 eV), exceptional thermal stability, and superior electrical conductivity, which operate by detecting changes in the electrical properties when exposed to target gases [9,10]. However, due to this simple operation mechanism, MOS-based sensors tend to respond to a wide range of volatile organic compounds (VOC) gases, resulting in low selectivity toward specific targets gas.

To address these limitations, researchers have developed techniques such as noble metal functionalization, doping, defect control, the formation of heterojunctions, and the use of novel nanomaterials to improve selectivity and sensitivity by tuning the potential barrier and employing catalytic activity [11–15]. Among these approaches, noble metals such as platinum (Pt), palladium (Pd), ruthenium (Ru), and silver (Ag) enhance the gas-sensing performance of MOS-based sensors through key mechanisms of electronic and chemical sensitization. A Schottky barrier forms at the interface between the metal and MOS, which amplifies changes in electrical conductivity by facilitating electron transfer (electronic sensitization). Additionally, the spillover effect of noble metals improves gas selectivity and response time (chemical sensitization) by facilitating the decomposition of specific gases on the metal surface. Notably, Pt is well known as a catalyst with superior chemical and mechanical stability compared to other metals and noble metals. Furthermore, the low binding energy of Pt catalysts makes them suitable candidates for realizing a highly selective C_2H_5OH sensor [16]. For example, Liu et al. synthesized SnO_2 nanoflowers decorated with Pt NPs using a hydrothermal technique, resulting in a 3.4-fold improvement in C_2H_5OH response at 320 °C compared to pure SnO_2 nanoflowers [17]. Similarly, Zhao et al. showed that doping SnO_2 hollow nanospheres with 0.3 wt% Pt NPs significantly enhanced C_2H_5OH sensing, with the gas response for 1 ppm H_2S increasing dramatically from 19 (pristine SnO_2) to 250 at 120 °C, highlighting the critical role of Pt in enhancing sensing performance [18]. Moreover, the dimensions and spatial arrangement of noble metal catalysts have a significant impact on gas sensing performance, yet few studies have systematically evaluated the effects of Pt NPs size and distribution.

Herein, we fabricated 1-dimensional In_2O_3 NRs with Pt NPs using a simple GLAD to improve gas response and selectivity. To determine the optimal initial Pt film thickness and operating temperature, we evaluated gas-sensing characteristics at various temperatures up to 450 °C. In_2O_3 NRs with 1 nm thick Pt NPs exhibited the highest gas response at 450 °C and showed enhanced selectivity towards C_2H_5OH compared to In_2O_3 NRs. Additionally, the DL in both dry air and 80 % RH were calculated to be 0.42 ppb and 6.1 ppb, respectively, demonstrating the potential strategy for integration into IIDs applications.

2. Experimental section

2.1. Sample fabrication

Au interdigitated electrodes (IDEs), serving as substrates for gas sensors, were fabricated using a photolithography process. A Si wafer with a 3000 Å dry oxide layer was cleaned sequentially in a sonicator using CH_3COCH_3, isopropanol, and deionized (D.I.) water, 5 min per step. A photoresist layer (LOR 5A, MicroChem Corporation) was then spin-coated onto the Si wafer at 3000 rpm for 30 s and baked at 180 °C for 5 min. An additional photoresist layer (AZ GXR 601, AZ Electronic Materials) was subsequently spin-coated under the same conditions. After a 1-minute bake at 150 °C, the IDEs were patterned using a mask aligner system (MDA-400S, MIDAS System). The Si wafer was then developed (AZ 300MIF, MicroChemicals), rinsed with D.I. water, and placed in an e-beam evaporator (EBX-1000, ULVAC) for deposition of an Au/Pt/Cr layer (180 nm/70 nm/30 nm). The Au-IDE-patterned substrate was cleaned again in a sonicator with CH_3COCH_3, C_2H_5OH, and D.I. water, for 5 min per step. Afterward, the samples were transferred to an electron beam evaporator (Korea Vacuum Tech) for deposition of a 600 nm-thick In_2O_3 NRs film (99.99 %, Taewon Scientific Co.). The deposition was carried out at a glancing angle (80°) with a rotation speed of 6 rpm, a base pressure of 3×10^{-6} Torr, and a growth rate of 1 Å/s. To crystallize the In_2O_3 NRs, the sample was annealed in a box furnace with a temperature ramp of 5 °C/min up to 500 °C, holding at this temperature for 1 h in ambient air. For Pt NP decoration on the top surface of the In_2O_3 NRs, a Pt film (0.5, 1, or 2 nm thick; 99.99 %, Taewon Scientific Co.) was deposited at the base position (0°) with a deposition rate of 0.1 Å/s. The Pt film-deposited In_2O_3 NRs were then annealed again (5 °C/min, 500 °C, 1 h) to transform the Pt film into Pt NPs, resulting in In_2O_3 NRs with Pt NPs.

2.2. Characterization

The top-view and cross-sectional morphologies of the In_2O_3 NRs with Pt NPs were analyzed using field-emission scanning electron microscopy (FE-SEM; JSM-7610F-Plus, JEOL) at an acceleration voltage of 15 kV and a working distance of 8 mm and high-resolution transmission electron microscopy (HR-TEM; JEM-ARM 200F NEOARM, JEM-F200, JEOL). The surface FE-SEM images were analyzed using MATLAB R2023a (MathWorks, Natick, MA, USA), and custom scripts were written to calculate the porosity. The crystal structures of the In_2O_3 NRs and Pt NPs were obtained using X-ray diffraction (XRD; Empyrean, PANalytical) with Cu-Kα radiation ($\lambda = 1.5418$ Å), a tube voltage of 40 kV, and a current of 30 mA.

2.3. Gas-Sensing measurement

The gas sensing measurement setup consisted of a mini probe chamber equipped with an 8-channel probe system (Fig. S1, MPS4000, PHOCOS), a gas controller (PHOCOS) for accurate adjustment of gas concentration between 1 and 50 ppm, and a temperature controller (PHOCOS). The sensing chamber had dimensions of 140 mm in width, 80 mm in length, and 40 mm in height. Gases were sequentially injected in alternating cycles of dry air and target gases (C_2H_5OH, HCHO, C_3H_8, C_5H_8, C_7H_8, H_2, NH_3, CH_4, and H_2S; balanced with dry air, RIGAS) through an automated gas control system. A silicon carbide heater maintained the operating temperature at 150 °C, 200 °C, 250 °C, 300 °C, 350 °C, 400 °C, and 450 °C to assess the gas-sensing properties of the sensors across various temperatures. The gas response was evaluated using a source meter (Keithley 237, KEITHLEY) under a constant DC bias voltage of 1 V, while the sensor resistance was measured with high accuracy using the 7001 switch system (KEITHLEY). Resistance changes were monitored at intervals of 2 s to evaluate the response to the target gases.

3. Results and discussion

3.1. Characterization of In_2O_3 NRs with Pt NPs

The transducer function in gas sensors refers to the process by which chemical interactions between gas molecules and the sensing material are converted into measurable electrical signals. Previous studies have reported that nanostructures enhance this transducer function by increasing the surface area and providing more active sites for gas interactions, thereby improving sensor performance [19]. Additionally, nanostructures often form multiple neck regions where grains or particles connect which are highly sensitive to changes in electrical signals and further amplify the sensor's response to gas adsorption. To maximize these effects, we fabricated one-dimensional NRs structures using electron beam evaporation through the GLAD technique at an 80° angle

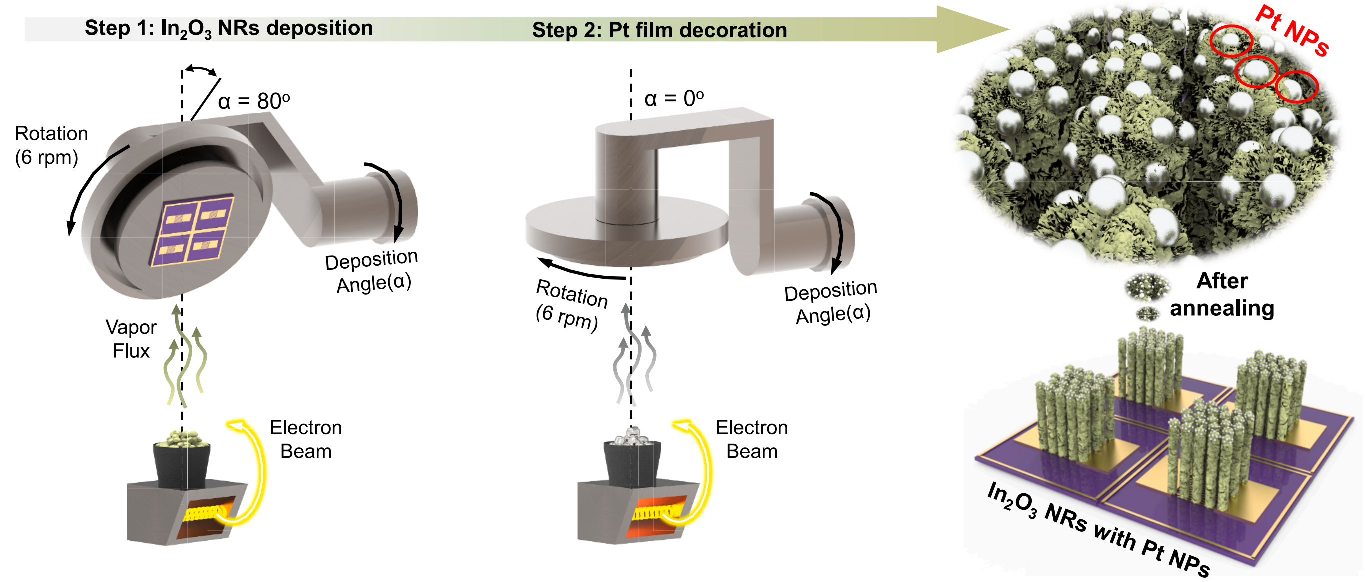

Fig. 1. A schematic representation of the fabrication procedure for a gas sensor based on In_2O_3 NRs with Pt NPs.

(Fig. 1). The GLAD technique operates by positioning the substrate at a high angle relative to the incoming vapor flux, resulting in a self-shadowing effect. This effect occurs when the elevated regions of the growing structures block vapor from reaching certain areas, promoting anisotropy and guiding the growth of columnar structures like NRs [20,21]. To decorate the In_2O_3 NRs with Pt NPs, the substrate was positioned at a base angle of 0°, and Pt film were deposited at thicknesses of 0.5, 1, and 2 nm. A subsequent annealing process was applied to promote the crystallization of the In_2O_3 and induce the aggregation of the Pt film into Pt NPs simultaneously, finalizing the formation of In_2O_3 NRs with Pt NPs.

Fig. 2 presents the surface and cross-sectional FESEM images, the transmission electron microscopy (TEM) image, along with X-ray diffraction (XRD) analysis results of In_2O_3 nanorods (INRs) and In_2O_3 NRs with different Pt NPs (PINRs). The Pt film was first deposited at different initial thicknesses of 0.5, 1, and 2 nm, referred to as 0.5-PINRs, 1-PINRs, and 2-PINRs, respectively. The deposition mechanism through GLAD provides highly porous nanostructures, as confirmed by the top surface FE-SEM images (Fig. 2a–d). Each porosity was calculated by binary digitization of the SEM images and found to be 61.8 %, 61.4 %, 61.2 %, and 61.0 % for INRs, 0.5-PINRs, 1-PINRs, and 2-PINRs, respectively. This indicates that the overall porosity decreased as the initial Pt film thickness increased. The deposited INRs were grown with an approximate height of 600 nm, perpendicular to the substrate (Fig. 2e–h). The INRs exhibited a sharp, elongated shape, leading to the formation of numerous necks between the structures, with no noticeable changes in total thickness observed with varying initial Pt film thicknesses.

To analyze the detailed structure of the 1-PINRs, a cross-sectional scanning transmission electron microscopy (STEM) image was obtained. The STEM image shows both the grain sizes of In_2O_3 and Pt NPs, indicating that 1-PINRs are porous structure (Fig. 2i). The HRTEM images are displayed in Fig. 2j, with magnified views provided in Fig. 2k–l (In_2O_3 and Pt, respectively). The In_2O_3 lattice fringe is associated with the (400) plane, showing a fringe spacing of 0.25 nm, while the Pt lattice fringe is related to the (111) plane with a spacing of 0.23 nm, confirming the successful formation of Pt NPs [22,23].

Fig. 2m demonstrates conventional crystallinity of the In_2O_3 by showing the diffraction peaks at 21.4°, 30.6°, 35.4°, 37.8°, 41.9°, 45.7°, 51.1°, and 56.0° (PDF No. 00–044-1087). Additionally, the peak of deposited Pt observed at the 44-45° region corresponds to the (200) plane (PDF 00-033-0875). Collectively, it is clear that the INRs were effectively crystallized during the annealing process, with the Pt film aggregating into Pt NPs and no additional phase formation observed throughout the process.

3.2. Gas sensing properties of INRs and PINRs

The MOS-based gas sensors interact with target gases through the adsorbed oxygen species (O_2^-, O^-, or O^{2-}) on the surface of MOS, which generates an electrical depletion layer (EDL) at n-type MOS the surface [24]. This reaction is significantly influenced by the operating temperature, as the type of adsorbed oxygen species varies with temperature. At temperatures below 100°C, O_2^- is predominantly formed. Between 100°C and 300°C, O^- becomes the dominant species, while at temperatures above 300°C, the more reactive O^{2-} species are primarily present. When reducing gases, such as CH_3COCH_3, HCHO, and C_5H_8, react with the adsorbed oxygen ions on the n-type MOS surface, electrons are injected into the material, thereby reducing the resistance of sensors. In these reactions, the gas response (S) of gas sensors was defined using the ratio of saturated resistance in air (R_a) to resistance in target gas (R_g), as represented by equation:

$$S = (R_a - R_g)/R_g \tag{1}$$

The decorated Pt NPs on the top surface of INRs form a Schottky barrier between the Pt-In_2O_3 interface, leading to the expansion of the EDL. The size and distribution of Pt NPs also significantly affect the gas sensing properties of all PINRs due to arrangement of EDL. To find optimal operating temperature and Pt film thickness, INRs and all PINRs were exposed to 50 ppm C_2H_5OH at different temperatures (150, 200, 250, 300, 350, and 450 °C), as shown in Fig. 3a–g. Upon exposure to the C_2H_5OH as a reducing gas, all samples show a decrease in resistance, followed by a recovery to R_a, indicating n-type semiconductor behavior. As the temperature increased, the R_a of INRs and all PINRs gradually increased, reaching maximum values at 400°C for INRs and 450°C for all PINRs. Compared to INRs, all PINRs exhibited higher R_a values at all tested temperatures due to the expanded EDL induced by the Schottky junctions, with 1-PINRs showing the maximum R_a. To clearly confirm the optimal conditions and sample, Fig. 3h shows the responses as a function of Pt film thickness. Similar to R_a, maximum values of response indicate at 400°C and 450°C for INRs and all PINRs, respectively. At 450°C, the responses were 3.04, 21.39, 36.98, and 21.37 for INRs, 0.5-PINRs, 1-PINRs, and 2-PINRs, respectively, with 1-PINRs exhibiting the

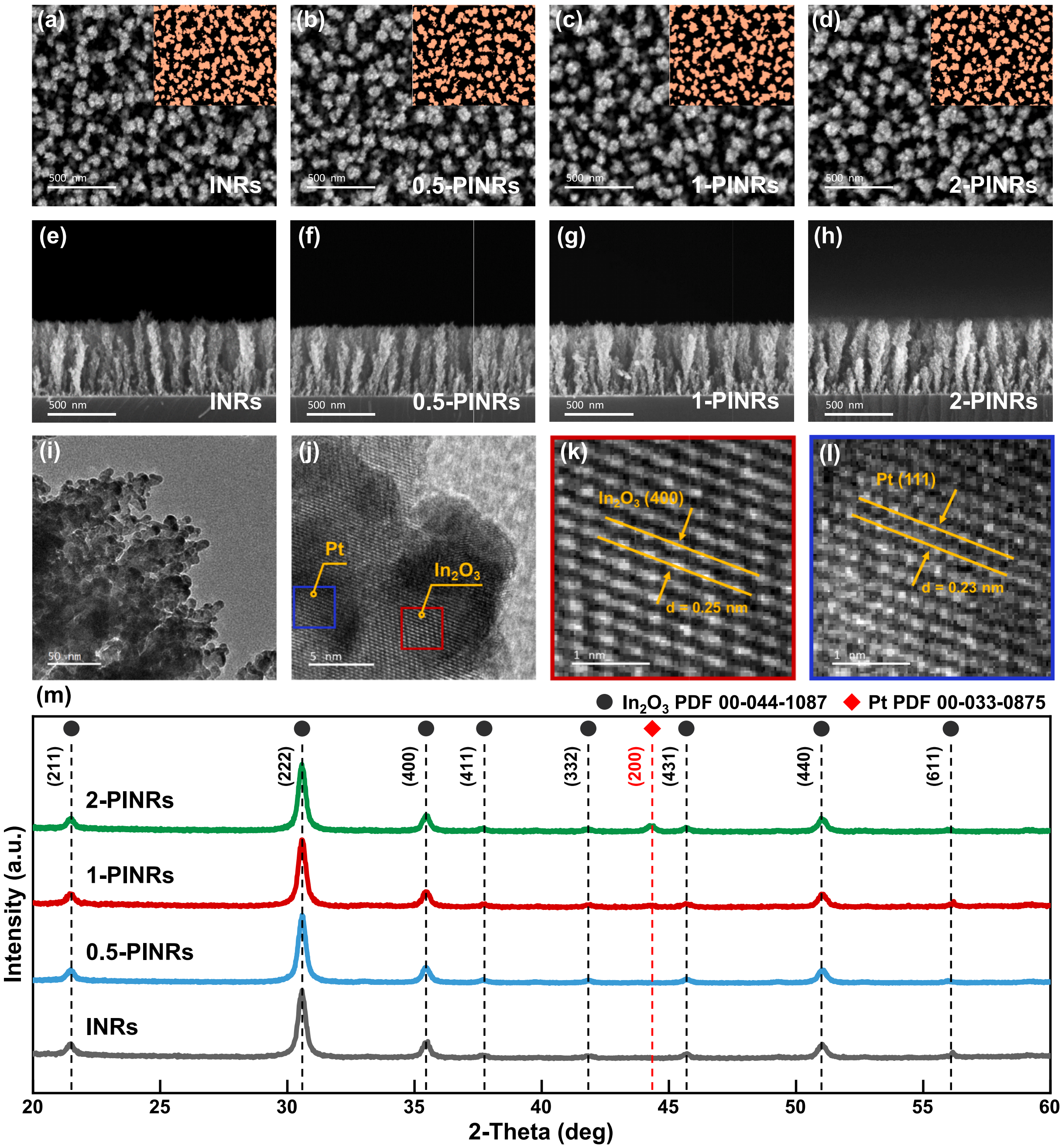

Fig. 2. Top-view SEM micrographs of (a) INRs and (b-d) 0.5-PINRs, 1-PINRs, 2-PINRs, respectively. The inset shows the converted top-view SEM images by MATLAB. (e-h) Cross-sectional SEM images of INRs and PINRs. (i) STEM image showing the top region of 1-PINRs; (j) HRTEM image of 1-PINRs; (k-l) magnified views of the selected areas, with corresponding to In_2O_3 and Pt respectively. (m) XRD patterns for INRs and PINRs.

highest response. Interestingly, the R_a and response of INRs decreased at 450 °C, which will be discussed in detail in future sections.

Since IIDs required selectively detect C_2H_5OH in human breath, which includes various gases, such as NH_3, CH_4, and H_2S, we investigate selectivity of INRs and 1-PINRs by exposing them to 50 ppm C_2H_5OH, HCHO, C_3H_8, C_5H_8, C_7H_8, H_2, NH_3, CH_4, and H_2S at 450 °C (Fig. S2). The 1-PINRs show response values of 37.0, 21.7, 2.1, 14.1, 10.9, 3.2, 4.7, 2.4, and 20.1 for C_2H_5OH, HCHO, C_3H_8, C_5H_8, C_7H_8, H_2, NH_3, CH_4, and H_2S, respectively, whereas the INRs exhibited responses of 3.0, 4.0, 1.1, 3.8, 2.1, 2.3, 1.8, 1.0, and 6.6 for the same gases, indicating that 1-PINRs have enhanced response across all target gases. To clearly evaluate the gas selectivity and the effects of Pt NPs, the radar plots of response for INRs (S_{INRs}) and 1-PINRs (S_{PINRs}) to all exposed gases were obtained, as shown in Fig. 4a–b. The INRs exhibited the highest response to H_2S, followed by HCHO, C_5H_8, C_2H_5OH, H_2, C_7H_8, NH_3, C_3H_8, and CH_4. Meanwhile, the highest response of 1-PINRs change to C_2H_5OH from H_2S at INRs, followed by HCHO, H_2S, C_5H_8, C_7H_8, NH_3, H_2, C_3H_8, and CH_4. H_2S showed the third-highest response of 6.6 for 1-PINRs, which exhibited the highest response of 20.1 for INRs. The C_2H_5OH response of 37.0 for 1-PINRs was approximately 37 times higher than the lowest response of 1 observed for CH_4. To investigate the effect of Pt NPs, we calculated S_{INRs}/S_{PINRs} value which indicate approximately 12 as highest value to C_2H_5OH followed by HCHO, C_7H_8, C_5H_8, NH_3, H_2S, NH_3, CH_4, C_3H_8 (Fig. 4c). Compared to S_{INRs}/S_{PINRs} values for other gases, which range between 1 and 5, C_2H_5OH exhibits a remarkable improvement. As shown in Fig. 4d, we calculated response time (t_{res}, 90 % of the response)) for INRs and 1-PINRs, with 1-PINRs achieving lower $t_{90\%}$ to all exposed gases compared to INRs. Especially, $t_{90\%}$ decreased by

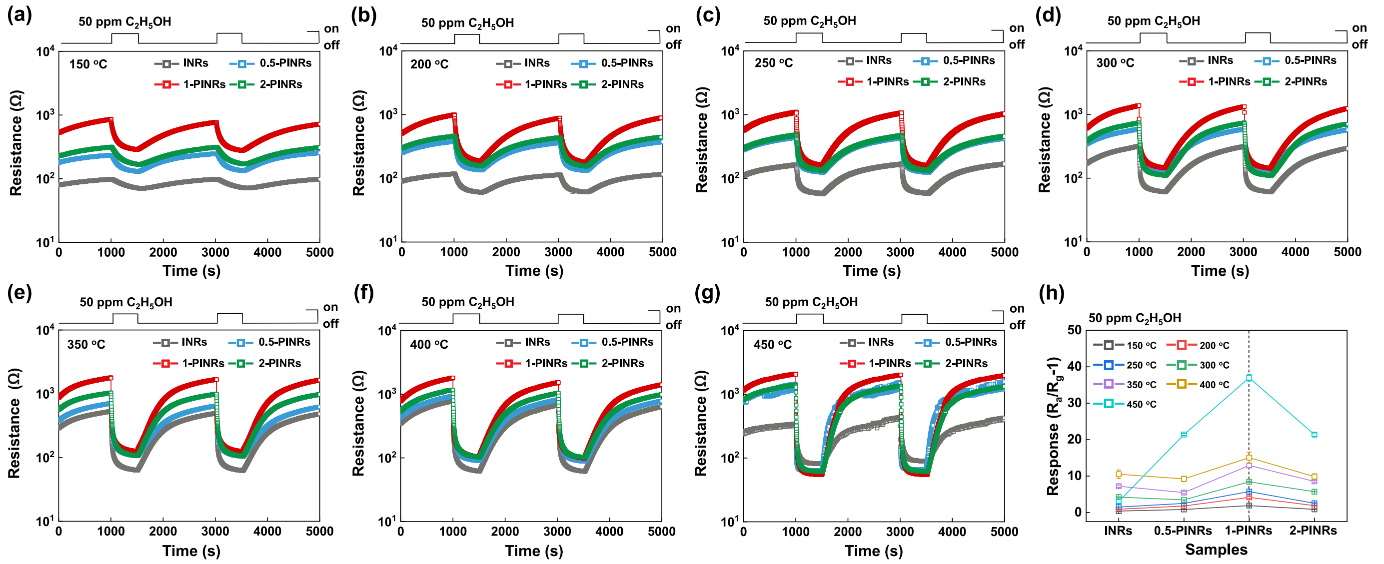

Fig. 3. Resistance curves of the INRs, 0.5-PINRs, 1-PINRs, and 2-PINRs to 50 ppm C_2H_5OH at different temperatures; (a) 150 °C, (b) 200 °C, (c) 250 °C, (d) 300 °C, (e) 350 °C, (f) 400 °C, and (g) 450 °C. (h) Gas responses to C_2H_5OH of INRs, 0.5-PINRs, 1-PINRs, and 2-PINRs-based gas sensors at different temperatures.

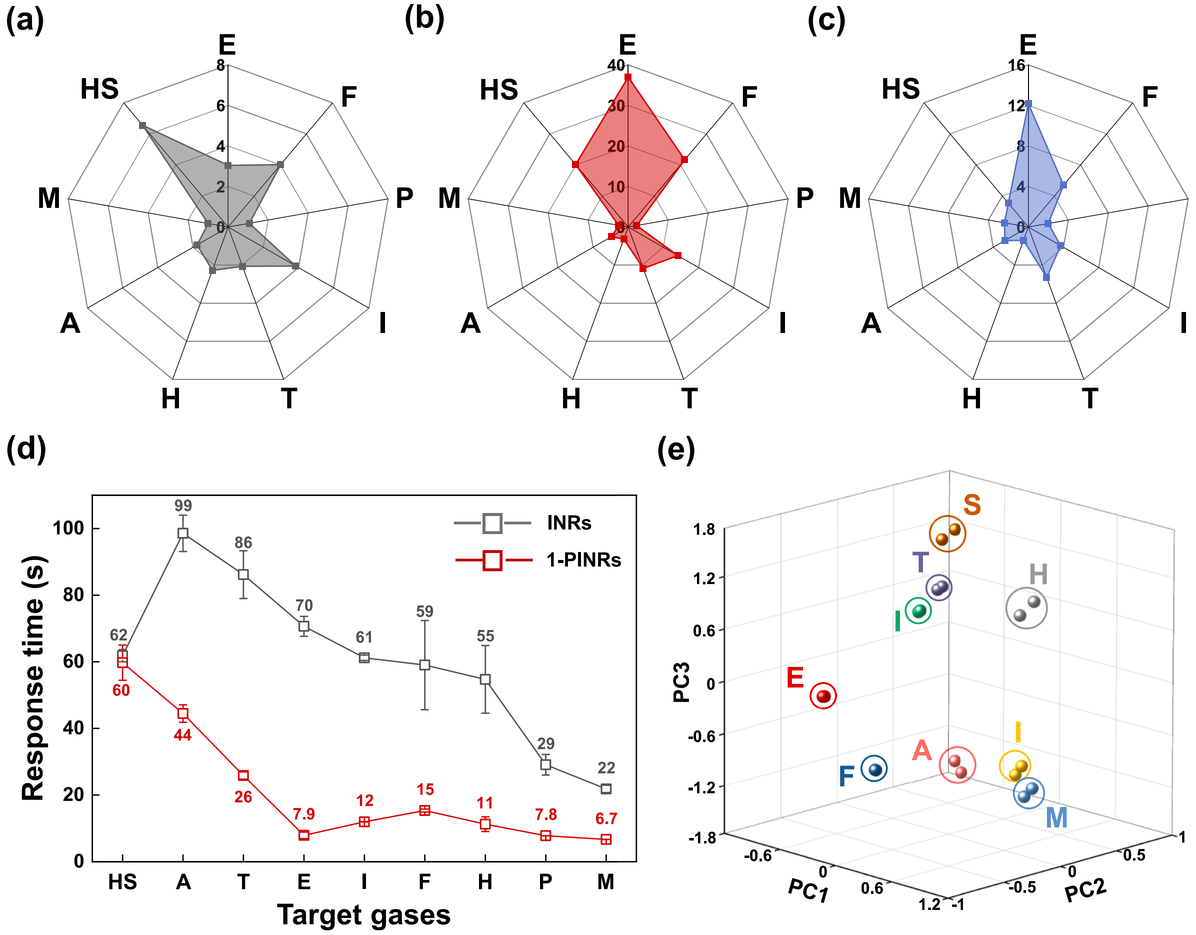

Fig. 4. Radar plot of responses of (a) INRs and (b) 1-PINRs to 50 ppm various gases at 450 °C (E: C_2H_5OH, F: HCHO, P: C_3H_8, I: C_5H_8, T: C_7H_8, H: H_2, A: NH_3, M: CH_4, and HS: H_2S). (c) The response ratios (S_{PINRs} / S_{INRs}) between INRs and 1-PINRs. S_{INRs} and S_{PINRs} represent the gas responses of INRs and 1-PINRs, respectively. (d) t_{res} of INRs and 1-PINRs. (e) 3D PCA graphs based on the results of base resistance, target gas resistance, response, response time, and recovery time of two repeated measurements to nine gases for 1-PINRs.

approximately 62 s (from 70 s to 7.9 s) for C_2H_5OH, representing the most significant reduction among all exposed gases. To further enhance gas selectivity, we performed principal component analysis (PCA) based on R_a, R_g, S, t_{res}, and recovery time (t_{rec}, 90 % of the original state) of each response curve (Fig. 4e). Data points of each gas are distinctly separated and form clusters for the same gas, allowing the distinction of each target gas. Enhanced C_2H_5OH sensing performance like high response and selectivity and fast t_{res} attributed to electronic and chemical sensitization of Pt NPs, which will be discussed in detail within the following section.

For practical applications, both reliability and accuracy of the gas sensor are one of the most important factors. To confirm repeatability with long-term stability, the 1-PINRs were alternately exposed to air and 50 ppm of C_2H_5OH over 20 cycles (Fig. 5a). During the 20 cycles, the 1-PINRs fully recovered to their initial resistance after the multiple exposures to target gases. To quantify the differences in response for 20 curves, the standard deviation (σ) was 41.63. To consider relative magnitude of the σ in comparison to the mean (μ), coefficient of variation (C.V.) was calculated 2.73 % based on the following equations:

$$C.V. = \frac{\sigma}{\mu} \tag{2}$$

Additionally, the response of the 1-PINRs to 50 ppm of C_2H_5OH was measured over a period of 10 days at 24-hour intervals to evaluate reliability, with the C.V. was calculated to be 5.26 % (Fig. 5b-l). Compared to commercial gas sensors, which typically exhibit C.V. values between 16.7 % and 41 %, our results demonstrate that the 1-PINRs possess significant potential for commercialization [25,26]. In addition, we investigated the humidity dependence of the 1-PINRs, finding that both R_a and gas response progressively decreased with increasing humidity. Notably, the response at 80 % RH was reduced to approximately 16 % of that under dry conditions (Fig. S3). Despite this degradation, the 1-PINRs maintained a high gas response of 6.15, highlighting their robustness under varying humidity conditions.

To calculate the DL of C_2H_5OH, the 1-PINRs were tested under both dry and 80 % RH conditions, with exposure to multiple pulses of C_2H_5OH at concentrations ranging from 3 ppm to 7 ppm (Fig. 6). In both dry and 80 % RH conditions, the response linearly increased with increasing gas concentration, indicating exceptional linearity and stability. Under dry conditions, the sensor responses were 9.9, 11.6, 13.8, 15.6, and 17.1 for 3, 4, 5, 6, and 7 ppm C_2H_5OH, respectively, while in 80 % RH, response values were 2.0, 2.3, 2.7, 3.0, and 3.5. After measuring the slope in a linear fit plot of response and concentration, the DL was then determined using a signal-to-noise ratio of 3, based on the following equations [27]:

$$R_{x^2} = \sum (y_i - y)^2 \tag{3}$$

$$RMS_{noise} = \sqrt{\frac{R_{x^2}}{N}} \tag{4}$$

$$\mathrm{DL} = 3\frac{RMS_{Noise}}{\mathrm{Slope}} \tag{5}$$

here, y_i represents discrete values from the response curve before C_2H_5OH exposure, and y is their average. The R_{x^2} value was obtained through a fifth-order polynomial fitting, using ten data points extracted from y_i. The root mean square (RMS_{noise}) was calculated from these values, where N indicates the number of data points. These calculations yielded a slope of 1.84 ppm^{-1} and a DL of 0.42 ppb under dry conditions (Fig. 6a), while under 80 % RH, the slope was 0.37 ppm^{-1}, with a DL of 6.1 ppb (Fig. 6b).

Considering that IIDs standards typically require DL over 200 ppb, particularly for monitoring the C_2H_5OH concentrations in exhaled breath, despite the reduced sensor response in humid conditions, the sufficient DL of 6.1 ppb under 80 % RH can offer powerful solution for being integrated into the IIDs as driver safety applications.

3.3. Surface chemical states of INRs and PINRs

Fig. 7 presents the XPS analysis INRs, 0.5-PINRs, 1-PINRs, and 2-PINRs to investigate the influence of chemical state, including oxygen species and the ionic states of Pt and In, on gas sensor performance. As shown in Fig. 7a, the In3d spectra displayed peaks at 444.4 eV and 452.0 eV, corresponding to $In3d_{5/2}$ and $In3d_{3/2}$, respectively [28]. After Pt deposition, the In3d peaks exhibited a shift toward lower binding energies, which can be attributed to electron transfer from In_2O_3 to Pt. The extent of the binding energy shift was found to increase with Pt film thickness, reaching a maximum value of 0.6 eV for the 2-PINRs. Fig. 7b illustrates the Pt4f spectra of PINRs with varying Pt decoration thicknesses. Five distinct peaks were observed at 71.1, 72.4, 74.4, 75.5, and 77.5 eV, corresponding to Pt^0, Pt^{2+}, the overlap of Pt^0 and Pt^{4+}, Pt^{2+}, and Pt^{4+}, respectively [29–32]. Notably, we observed an increase in the intensity of oxidized Pt states (Pt^{2+} and Pt^{4+}) for the 2-PINRs, suggesting that higher Pt thickness promotes oxidation, which could influence its sensing performance. Furthermore, the valence states of oxygen species in INRs and PINRs with varying Pt decoration thicknesses were analyzed using the O1s spectra, as shown in Fig. 7c. Three distinct peaks were observed, corresponding to lattice oxygen in the oxide (O_a, 529.2 eV), adsorbed oxygen ions related to oxygen defects (O_b, 530.2 eV), and surface hydroxyl groups (O_c, 531.4 eV) [33–35]. Among the various oxygen species, adsorbed oxygen ions play a particularly critical role in semiconductor-based gas sensors [36]. These adsorbed oxygen ions were actively involved in gas-sensing reactions, interacting with target gas molecules and significantly affecting sensor performance. Therefore, we calculated the ratio of O_b to the total oxygen species ($O_a + O_b + O_c$) and presented the results in Fig. 7d. Interestingly, the 1-PINR sample exhibited the highest ratio of adsorbed oxygen, which we interpret as an indication of the largest number of defect sites available for adsorption and desorption processes. These findings are consistent, where 1-PINRs demonstrated higher gas response compared to 0.5-PINRs and 2-PINRs.

3.4. Structural and catalytic effect of PINRs

Our results clearly demonstrate that the PINRs significantly improve gas sensing performance. We obtained two key effects of the PINRs, including structural effects and catalytic effects. Firstly, the large specific surface area of INRs enhanced both the transducer function and the utility factor, translating signals from chemical adsorption on the oxide surface into electrical signals and indicating the capacity of MOS grains to interact with target gases, respectively. In addition, the sharp and elongated shape of the INRs forms numerous necks (15–40 nm) that are integrated into current pathways, influencing more efficient resistance changes when exposed to target gases (Fig. S4). Secondly, the catalytic effects of Pt NPs can derive two mechanisms, namely electronic and chemical sensitization which improved the receptor function. Electronic sensitization is caused by the interaction between the Pt and In_2O_3 surface. Due to the difference in their work functions, electron transfer occurs from In_2O_3 to Pt until the Fermi levels equilibrate, which extends the EDL on the In_2O_3 surface and enhances gas response (Fig. 8a) [37]. At the narrow necks, this effect is further enhanced, resulting in a significantly higher response (Fig. 8b–c). The distribution and size of Pt NPs are crucial factors that significantly affect the gas sensing performance of PINRs. Our previous study showed that the initial film thickness resulted in different sizes and distributions of NPs, with optimal performance achieved at a specific film thickness [38]. For the thick Pt film (2-PINRs), the size and distribution of Pt NPs are relatively large and sparse, which cannot be utilized for the catalytic effects because the surface area of sensing material to react with target gases decreases and the widths of the interfacial EDL were not overlapped (Fig. 8d). On the other hand, when the thickness of Pt film (0.5-PINRs) is extremely thin, the Pt NPs are too dense and thus the surface area of In_2O_3 for the

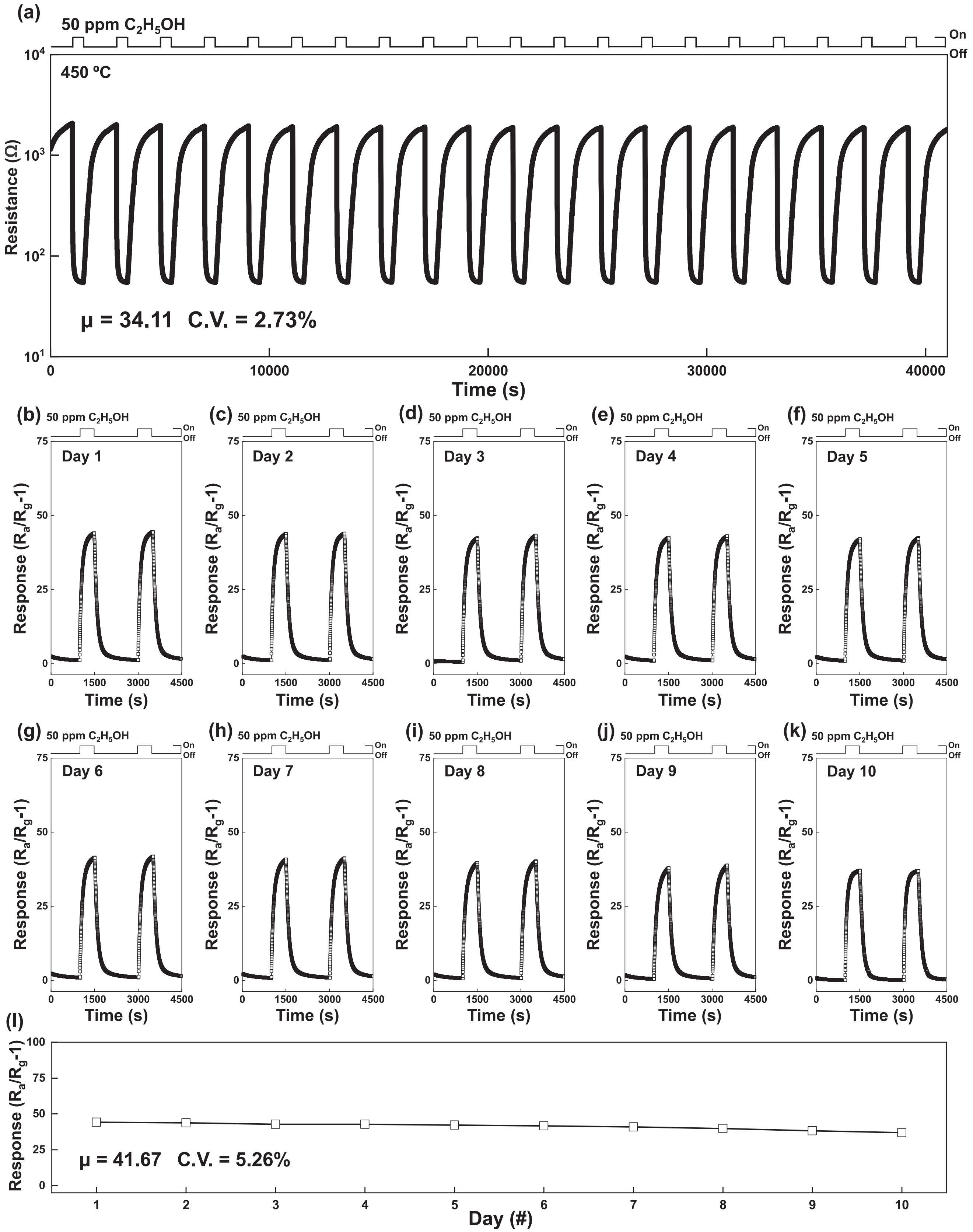

Fig. 5. (a) Resistance curves of 1-PINRs to 50 ppm C_2H_5OH at 450 °C measured over 20 cycles. (b-k) Response curves of 1-PINRs to 50 ppm C_2H_5OH at 450 °C analyzed over 10 days. (l) The response of 1-PINRs to 50 ppm C_2H_5OH at 450 °C over the measurement period.

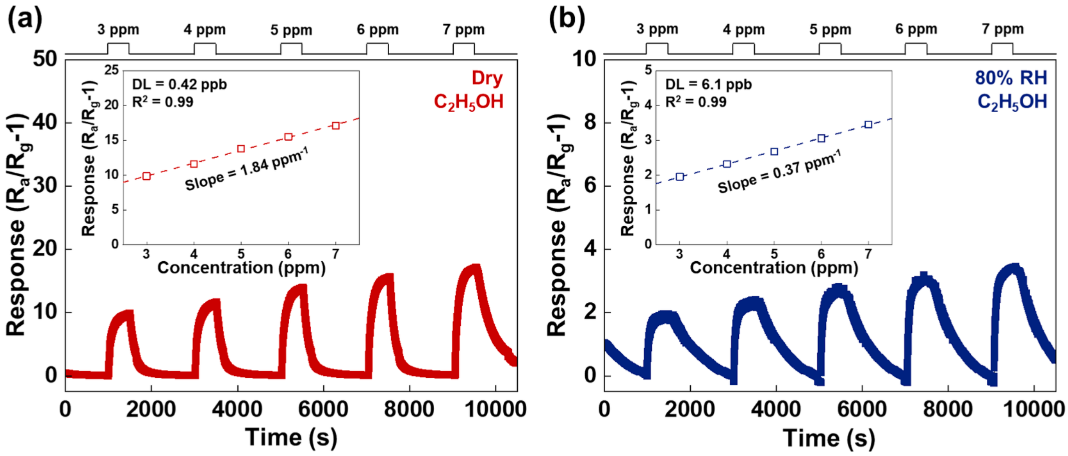

Fig. 6. Sensing curves of 1-PINRs toward low concentration C_2H_5OH (3, 4, 5, 6, and 7 ppm) in different conditions with (a) dry and (b) 80 % RH at 450 °C. The inset shows responses of 1-PINRs as a function of C_2H_5OH concentration under dry and 80 % RH, including the calculation of the DL.

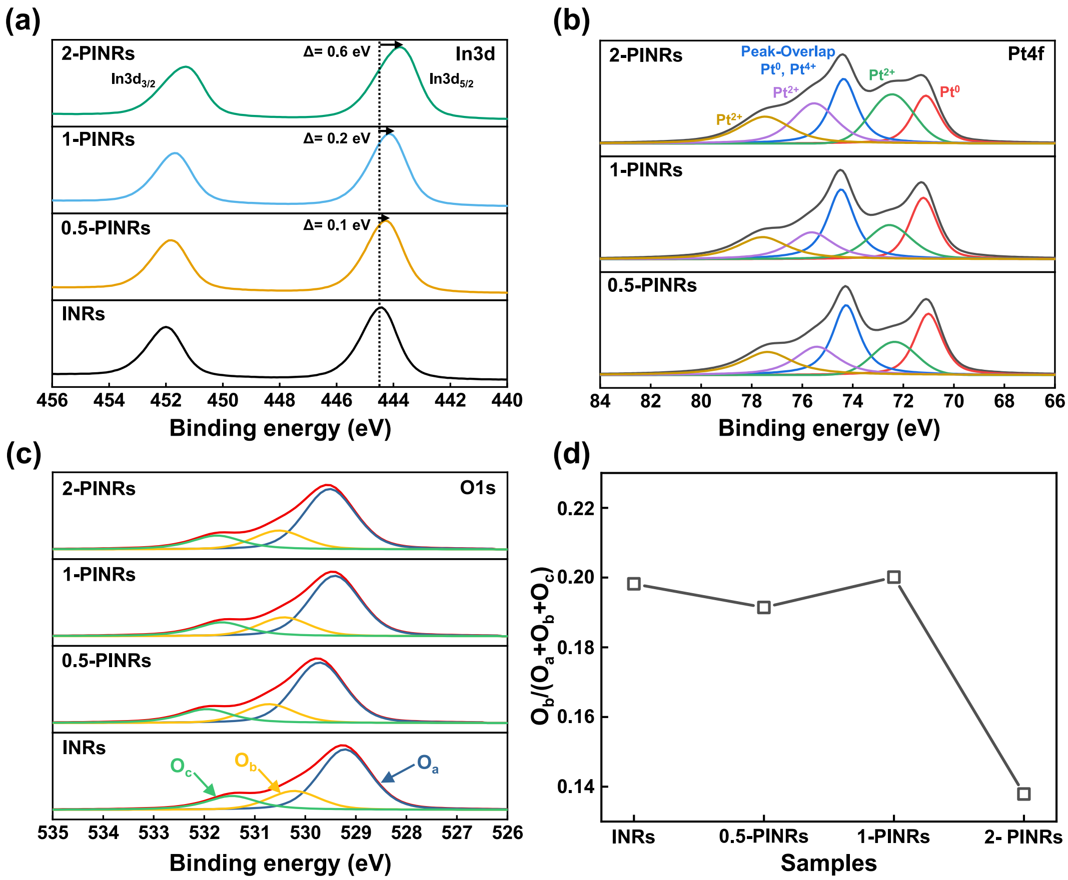

Fig. 7. XPS spectra of INRs, 0.5-PINRs, 1-PINRs, and 2-PINRs; (a) In3d spectra for both INRs and PINRs, (b) Pt4f spectra of PINRs and (c) O1s spectra for INRs and PINRs. (d) $O_b/(O_a + O_b + O_c)$ ratio of INRs, 0.5-PINRs, 1-PINRs, and 2-PINRs.

adsorption of gas molecules is significantly reduced, resulting in a low response relatively. Therefore, our results suggest that 1-PINRs possess an optimal size and distribution of Pt NPs. The chemical sensitization effect of Pt NPs plays a critical role in dissociation of gas molecules, such as C_2H_5OH. For instance, 1-PINRs exhibited a response time of 7.9 s compared to 70 s for INRs to 50 ppm C_2H_5OH at 450 °C, representing the most significant decrease among the target gases. The decrease in response time experimentally indicates the chemical sensitization effect of Pt NPs toward C_2H_5OH. Moreover, to clearly observe this effect, we introduced the Arrhenius equation:

$$S = \exp\left(-\frac{E_a}{kT}\right) \tag{6}$$

In this equation, E_a, k, and T represent the activation energy, Boltzmann constant, and operating temperature, respectively [39]. The activation energy was calculated as 32.18, 24.75, 22.27, and 25.85 kJ/mol for INRs, 0.5-PINRs, 1-PINRs, and 2-PINRs, respectively. As Pt NPs were decorated, the activation energy decreased, with 1-PINRs showing the lowest activation energy of 22.3 (Fig. 8e-f). R. Costa-Amaral et al. reported that DFT studies on Pt (111) surfaces revealed significant

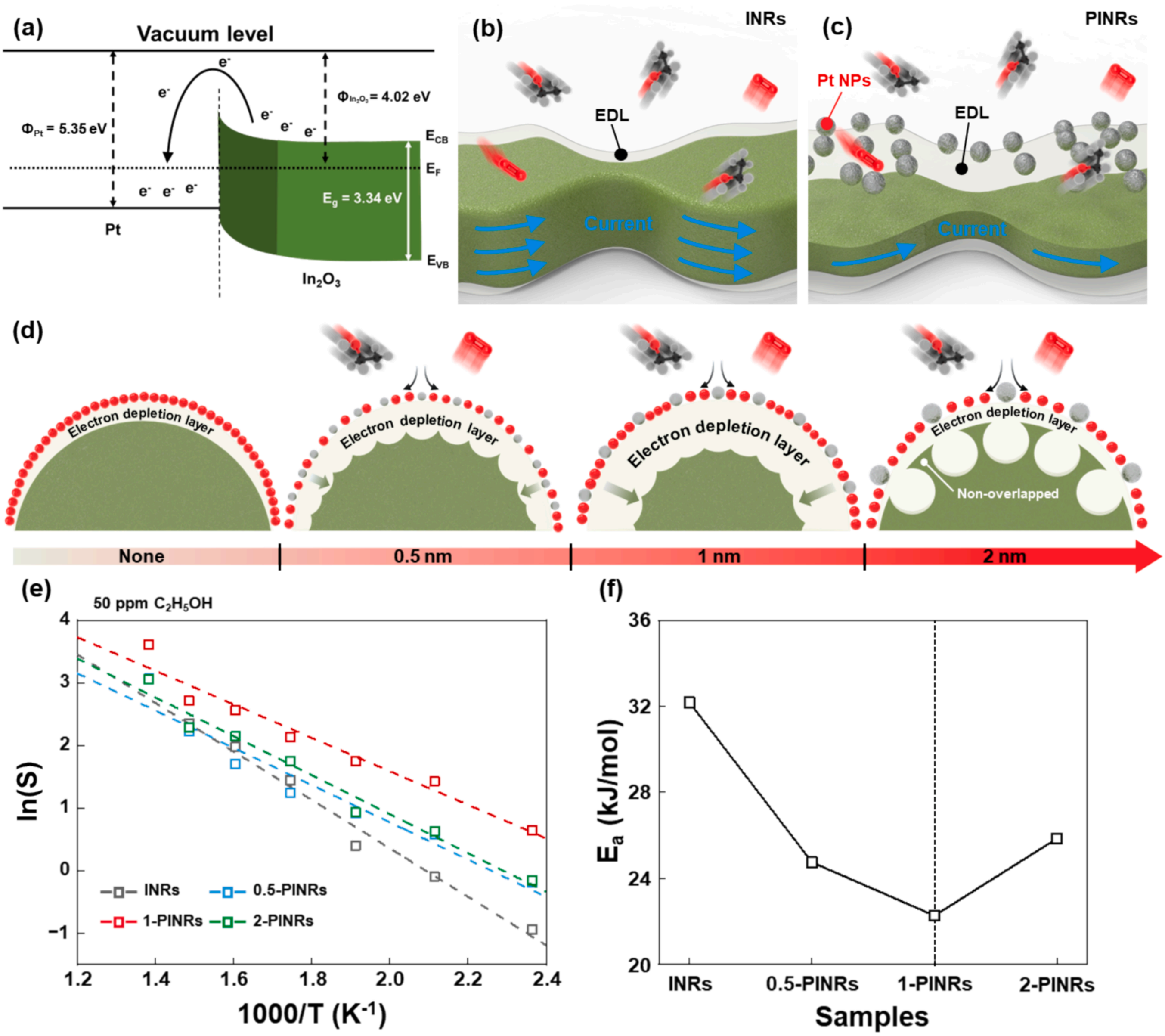

Fig. 8. (a) The energy band structure of Pt/In_2O_3 junctions, illustrating the formation of the EDL in the narrow necks between the NRs; (b) INRs and (c) PINRs. (d) Effect of Pt NPs size on the EDL formation. (e) Plots of ln(S) vs. 1000/T (K) measured for the INRs, 0.5-PINRs, 1-PINRs, and 2-PINRs. (f) Calculated activation energy of INRs, 0.5-PINRs, 1-PINRs, and 2-PINRs.

changes in the electronic density distribution upon C_2H_5OH adsorption [40]. These findings support the observed chemical sensitization of Pt NPs in this study. Furthermore, the decomposition of C_2H_5OH during the gas sensing process can be described by the following reactions [41]:

$$C_2H_5OH(gas) + 6O^-(ads) \rightarrow 2CO_2 + 3H_2O + 6e^- \quad (7)$$

In summary, the large specific surface area of INRs enhanced both the transducer function and the utility factor, whereas the catalytic effects (electronic and chemical sensitization) of Pt NPs improved the receptor function [42]. The highest catalytic effect was observed at the optimal catalyst distribution (1-PINRs), with each effect being maximized for C_2H_5OH, thereby enabling highly selective gas detection.

4. Conclusions

We successfully developed high-performance C_2H_5OH gas sensors based on PINRs, utilizing the GLAD technique to optimize Pt NPs size and distribution. In_2O_3 NRs with an initial Pt thickness of 1 nm exhibited the greatest enhancement in C_2H_5OH response, achieving DL of 0.42 ppb in dry air and 6.1 ppb at 80 % RH at 450 °C, far surpassing the 200 ppb detection requirement for IIDs. These improvements are attributed to (i) the expansion of the EDL resulting from Schottky barrier formation (electronic sensitization) and (ii) the spillover effect of Pt NPs (chemical sensitization). The strategic engineering of PINRs, including optimized NPs size and operating temperature of sensors, enabled stable and highly selective C_2H_5OH detection even under high humidity. This work provides valuable insights into enhancing MOS-based gas sensor performance through noble metal functionalization, paving the way for the development of advanced C_2H_5OH sensors for IIDs and other gas detection applications.

CRediT authorship contribution statement

Jae Han Chung: Methodology, Investigation, Formal analysis, Data curation. **Eunsol Lee:** Methodology, Investigation. **Junho Hwang:** Investigation, Data curation. **Junha Park:** Methodology, Investigation.

Seungjong Hwang: Methodology, Investigation. **Dongwook Youm:** Methodology, Investigation. **Dohyeon Shin:** Methodology, Investigation. **Ki Chang Kwon:** Methodology, Investigation. **Soonmin Yim:** Methodology, Investigation. **Wooyoung Lee:** Methodology. **Donghwi Cho:** Writing – review & editing, Writing – original draft, Conceptualization. **Kwangjae Lee:** Writing – review & editing, Writing – original draft, Conceptualization. **Young-Seok Shim:** Writing – review & editing, Writing – original draft, Conceptualization.

Declaration of competing interest

The authors declare that they have no known competing financial interests or personal relationships that could have appeared to influence the work reported in this paper.

Acknowledgements

This work was supported by Korea Research Institute of Chemical Technology (KRICT) of the Republic of Korea (KS2521-10) and grants from the National Research Foundation of Korea (NRF) funded by the Korea Government (Ministry of Science and ICT) (2022M3H4A3053304 [MIST]). This research was supported by “Regional Innovation Strategy (RIS)” through the National Research Foundation of Korea (NRF) funded by the Ministry of Education (MOE)(2021RIS-004). This paper was supported by the Education and Research Promotion Program of KOREATECH in 2023. The authors thank the Cooperative Equipment Center at KOREATECH for assistance with SEM analysis.

Appendix A. Supplementary material

Supplementary data to this article can be found online at https://doi.org/10.1016/j.apsusc.2025.162618.

Data availability

Data will be made available on request.

References

[1] Harper, A. M., Drunk driving: existing programs fail to stop the problem., https://minds.wisconsin.edu/bitstream/handle/1793/79086/Harper,%20Andrew.pdf?sequence=1, 2019 (accessed 20 October 2024).
[2] R.J. Stringer, Policing the drunk driving problem: A longitudinal examination of DUI enforcement and alcohol-related crashes in the US (1985–2015), Am. J. Crim. Justice 44 (2019) 474–498.
[3] J.C. Fell, R.B. Voas, Mothers against drunk driving (MADD): the first 25 years, Traffic Inj. Prev. 7 (2006) 195–212.
[4] John McCurley, Ignition Interlock Devices: Costs and Requirements. Ignition Interlock Devices. DUI Driving Laws., https://www.schmidtandclark.com/ignition-interlock-cost, 2024 (accessed 20 October 2024).
[5] Michal Raninec, Overcoming the Technical Challenges of Electrochemical Gas Sensing., www.analog.com/en/resources/technical-articles/overcoming-the-technical-challenges-of-electrochemical-gas-sensing, 2019 (accessed 11 December 2024).
[6] D.R. Wijesinghe, M.A. Zobair, M. Esmaeelpour, A review on photoacoustic spectroscopy techniques for gas sensing, Sensors 24 (2024) 6577.
[7] F.A. Ali, D.K. Mishra, R. Nayak, B. Nanda, Solid-state gas sensors: sensing mechanisms and materials, Bull. Mater. Sci. 45 (2022) 15.
[8] J. Zhang, Z. Qin, D. Zeng, C. Xie, Metal-oxide-semiconductor based gas sensors: screening, preparation, and integration, PCCP 19 (2017) 6313–6329.
[9] S. Yang, H. Yin, Z. Wang, G. Lei, H. Xu, Z. Lan, H. Gu, Gas sensing performance of In_2O_3 nanostructures: a mini review, Front. Chem. 11 (2023) 1174207.
[10] G.B. Nam, J.-E. Ryu, T.H. Eom, S.J. Kim, J.M. Suh, S. Lee, S. Choi, C.W. Moon, S. J. Park, S.M. Lee, B. Kim, S.H. Park, J.W. Yang, S. Min, S. Park, S.H. Cho, H.J. Kim, S.E. Jun, T.H. Lee, Y.J. Kim, J.Y. Kim, Y.J. Hong, J.-I. Shim, H.-G. Byun, Y. Park, I. Park, S.-W. Ryu, H.W. Jang, Real-time tunable gas sensing platform based on SnO_2 nanoparticles activated by blue micro-light-emitting diodes, Nano-Micro Lett. 16 (2024) 261.
[11] S. Luan, J. Hu, M. Ma, J. Tian, D. Liu, J. Wang, J. Wang, The enhanced sensing properties of MOS-based resistive gas sensors by Au functionalization: a review, Dalton Trans. 52 (2023) 8503–8529.
[12] S. Xue, S. Cao, Z. Huang, D. Yang, G. Zhang, Improving gas-sensing performance based on MOS nanomaterials: a review, Materials, Materials 14 (2021) 4263.
[13] X. Ma, X. Cai, M. Yuan, Y. Qu, Y. Tan, F. Chen, Self-powered and flexible gas sensor using defect-engineered WS2/G heterostructure, Sens. Actuat. B 371 (2022) 132523.
[14] D. Kong, B. Hong, J. Xu, X. Peng, J. Li, H. Chen, S. Qiu, N. Zhang, X. Wang, P−n heterojunction construction and interfacial interaction mechanism: NiO/In_2O_3 formaldehyde gas sensors with excellent sensitivity and selectivity, Appl. Surf. Sci. 688 (2025) 162442.
[15] D.L. Kong, B. Hong, J.C. Xu, X.L. Peng, J. Li, N. Zhang, Y.X. Zeng, X.Q. Wang, MOF-derived $Ag_{0.16}/In_{1.95}Pr_{0.05}O_3$ sensors with ultra-high sensitivity, quick response and excellent selectivity to formaldehyde gas, Talanta 284 (2025) 127278.
[16] R.L.H. Freire, D. Guedes-Sobrinho, A. Kiejna, J.L.F. Da Silva, Comparison of the performance of van der waals dispersion functionals in the description of water and ethanol on transition metal surfaces, J. Phys. Chem. C 122 (2018) 1577–1588.
[17] Y. Liu, J. Huang, J. Yang, S. Wang, Pt nanoparticles functionalized 3D SnO_2 nanoflowers for gas sensor application, Solid State Electron. 130 (2017) 20–27.
[18] Y.-P. Sun, Y.-F. Zhao, H. Sun, F.-C. Jia, P. Kumar, B. Liu, Synthesis and room-temperature H_2S sensing of Pt nanoparticle-functionalized SnO_2 mesoporous nanoflowers, J. Alloy. Compd. 842 (2020) 155813.
[19] Z. Wang, L. Zhu, S. Sun, J. Wang, W. Yan, One-dimensional nanomaterials in resistive gas sensor: from material design to application, Chemosensors 9 (2021) 198.
[20] K. Robbie, M.J. Brett, Sculptured thin films and glancing angle deposition: growth mechanics and applications, J. Vac. Sci. Technol. A 15 (1997) 1460–1465.
[21] Y.G. Song, J.Y. Park, J.M. Suh, Y.-S. Shim, S.Y. Yi, H.W. Jang, S. Kim, J.M. Yuk, B.-K. Ju, C.-Y. Kang, Heterojunction based on Rh-decorated WO_3 nanorods for morphological change and gas sensor application using the transition effect, Chem. Mater. 31 (2019) 207–215.
[22] K.K. Pawar, J.S. Shaikh, S.S. Mali, Y.H. Navale, V.B. Patil, C.K. Hong, P.S. Patil, Hollow In_2O_3 microcubes for sensitive and selective detection of NO_2 gas, J. Alloy. Compd. 806 (2019) 726–736.
[23] J. Liu, W. Chen, T. He, Y. Fang, Z. Zhong, X. Wang, Z. Li, Y. Song, Lewis base sites of non-oxide supports boost oxygen absorption and activation over supported Pt catalysts, RSC Adv. 12 (2022) 12537–12543.
[24] M.V. Nikolic, V. Milovanovic, Z.Z. Vasiljevic, Z. Stamenkovic, Semiconductor gas sensors: materials, technology, design, and application, Sensors 20 (2020) 6694.
[25] Compact gas sensor, Membrapor. https://www.membrapor.ch/compact-gas-sensor/, (accessed 10 December 2024).
[26] S.M. Bonham, S. Miller, Clinical comparison of 99th percentile and 10% coefficient of variation cutoff values for four commercially available troponin I assays, Lab. Med. 40 (2009) 470–473.
[27] J. Hwang, S.-H. Park, Y.-S. Shim, S. Sohn, J.H. Chung, Y.-H. Cho, J. Lee, M. Choi, G. H. Lee, D. Cho, K. Lee, W. Lee, Fast and selective isoprene gas sensor: influence of polystyrene size and role of the Au catalyst on gas sensing properties, Sens. Actuat. B 422 (2025) 136500.
[28] R. Bashir, M.K. Bilal, A. Bashir, J. Zhao, S.U. Asif, W. Ahmad, J. Xie, W. Hu, A low-temperature solution-processed indium incorporated zinc oxide electron transport layer for high-efficiency lead sulfide colloidal quantum dot solar cells, Nanoscale 13 (2021) 12991–12999.
[29] N. Jiang, B. Huang, M. Wang, Y. Chen, Q. Yu, L. Guan, Universal and energy-efficient approach to synthesize Pt-rare earth metal alloys for proton exchange membrane fuel cell, Adv. Sci. 11 (2024) 2305110.
[30] Y.E. Jeong, P.A. Kumar, H.L. Choi, K.Y. Lee, H.P. Ha, Catalytic activity and thermal stability of Arc plasma deposited Pt nano-particles on CeO_2-Al_2O_3, J. Nanosci. Nanotechnol. 15 (11) (2015) 8494–8501.
[31] J. Golubović, L. Rakočević, D. Vasiljević Radović, S. Štrbac, Improved oxygen reduction on GC-supported large-sized Pt nanoparticles by the addition of Pd, Catalysts 12 (9) (2022) 968.
[32] L. Preethi, R.P. Antony, T. Mathews, S. Dash, A. Tyagi, Optical transmittance and electrocatalytic efficacy of chronoamperometrically and chronopotentiometrically deposited platinum electrodes for DSSC application, J. Nanosci. Nanotechnol. 16 (2016) 10087–10096.
[33] S. Sundaresh, S.D. Nehate, K.B. Sundaram, Electrical and optical studies of reactively sputtered indium oxide thin films, ECS J. Solid State Sci. Technol. 10 (2021) 065016.
[34] S. Liu, C. Sun, J. Chen, J. Xiao, J.-L. Luo, A high-performance ruddlesden–popper perovskite for bifunctional oxygen electrocatalysis, ACS Catal. 10 (2020) 13437–13444.
[35] J. Zou, J. Gao, Y. Wang, Synthesis of highly active H_2O_2-sensitized sulfated titania nanoparticles with a response to visible light, J. Photochem. Photobiol. A Chem. 202 (2009) 128–135.
[36] E. Ciftyurek, Z. Li, K. Schierbaum, Adsorbed oxygen ions and oxygen vacancies: their concentration and distribution in metal oxide chemical sensors and influencing role in sensitivity and sensing mechanisms, Sensors 23 (1) (2023) 29.
[37] W. Liu, Y. Xie, T. Chen, Q. Lu, S. Ur Rehman, L. Zhu, Sens. Actuat. B: Chem. 298 (2019) 126871.
[38] Y.-S. Shim, H.G. Moon, D.H. Kim, L. Zhang, S.-J. Yoon, Y.S. Yoon, C.-Y. Kang, H. W. Jang, Au-decorated WO_3 cross-linked nanodomes for ultrahigh sensitive and selective sensing of NO_2 and C_2H_5OH, RSC Adv. 3 (2013) 10452–10459.
[39] J. Lee, Y. Jung, S.-H. Sung, G. Lee, J. Kim, J. Seong, Y.-S. Shim, S.C. Jun, S. Jeon, High-performance gas sensor array for indoor air quality monitoring: the role of Au nanoparticles on WO_3, SnO_2, and NiO-based gas sensors, J. Mater. Chem. A 9 (2021) 1159–1167.

[40] R. Costa-Amaral, J.L.F. Da Silva, The adsorption of alcohols on strained Pt3Ni(111) substrates: a density functional investigation within the D3 van der Waals correction, PCCP 20 (2018) 24210–24221.

[41] C.T. Quy, N.X. Thai, N.D. Hoa, D.T. Thanh Le, C.M. Hung, N. Van Duy, N. Van Hieu, C_2H_5OH and NO_2 sensing properties of ZnO nanostructures: correlation between crystal size, defect level and sensing performance, RSC Adv. 8 (2018) 5629–5639.

[42] J. Shin, G. Lee, M. Choi, H. Jang, Y. Lim, G.-S. Kim, S.-H. Nam, S.-H. Baek, H.-C. Song, J. Kim, C.-Y. Kang, J.-O. Lee, S. Jeon, D. Cho, J.-S. Jang, Atomically mixed catalysts on a 3D thin-shell TiO_2 for dual-modal chemical detection and neutralization, J. Mater. Chem. A 11 (2023) 18195–18206.

Jae Han Chung is a combined bachelor-master's candidate under the supervision of Prof. Young-Seok Shim at School of Energy, Materials & Chemical Engineering at Korea University of Technology & Education (KOREATECH). His research interests are the fabrication of nanostructured metal oxide and their applications to various devices including sensor and electrochromic devices.

Eunsol Lee is currently a combined bachelor-master's candidate in the School of Energy, Materials & Chemical Engineering at Korea University of Technology & Education (KOREATECH) under the supervision of Prof. Young-Seok Shim. His research focuses on micro/nanostructured materials and their large-area synthesis methods for gas sensing applications.

Junho Hwang received a Master's degree in the Department of Mechanical Design Engineering from Kookmin University in 2018. Since 2020, He is currently a Ph.D. candidate in the Department of Materials Science and Engineering at Yonsei University under the supervision of Prof. Wooyoung Lee. His research focuses on micro/nanostructured materials and their large-area synthesis methods for gas sensing applications.

Junha Park is currently a bachelor's candidate in the School of Mechanical Engineering at Korea University of Technology & Education (KOREATECH).

Seungjong Hwang is currently a bachelor's candidate in the School of Energy, Materials & Chemical Engineering at Korea University of Technology & Education (KOREATECH).

Dongwook Youm is currently a bachelor's candidate in the School of Energy, Materials & Chemical Engineering at Korea University of Technology & Education (KOREATECH).

Dohyeon Shin is currently a bachelor's candidate in the School of Energy, Materials & Chemical Engineering at Korea University of Technology & Education (KOREATECH).

Ki Chang Kwon is a Senior Research Scientist at the Interdis-ciplinary Materials Measurement Institute at Korea Research Institute of Standards and Science (KRISS). He received his Ph. D. from the Department of Materials Science and Engineering at Seoul National University in 2018. He worked as a Post-doctoral research staff at the National University of Singapore (NUS) from 2018 to 2021. His research interests include the synthesis of low dimensional materials (1D & 2D), and halide perovskites, and their applications for nanoelectronics, solar water splitting catalysts, and chemical sensors.

Soonmin Yim is a Principal Researcher of the Advanced Materials Division at the Korea Research Institute of Chemical Technology (KRICT) in South Korea (2020~present). He received his Ph. D. degree in Materials Science and Engineering in 2018 from KAIST, and joined Pritzker School of Molecular Engineering (PME) at the University of Chicago (2018~2020) as a postdoctoral researcher. His research interest in process development of scalable and self-driven micro/nanofabrication techniques and applied them for various applications such as electronics and sensors.

Wooyoung Lee is the Underwood distinguished professor of the Department of Materials Science and Engineering at Yonsei University in Korea. He is also the Director of the Center for Super Critical Material Industrial Technology, National Core Materials Research Center and the institute of Korea Initiative for Fostering University of Research and Innovation. He is the President of The Korean Magnetics Society and a regular member of the National Academy of Engineering of Korea. In recent years, his research interests have centered on hydrogen sensors, various metal oxide semiconducting gas sensors, and breath analyzers. He is also studying rare-earth permanent magnets and thermoelectric materials and devices. He has received a number of awards in nano-related research areas including a Prime Minister Award (2023) in Nano Korea 2023, SeAH-Haiam Fellowship Award (2018) in The Korean Institute of Metals and Materials and a Service Merit Medal (2008) from the Government of Korea due to his contribution to the development of intellectual properties. He has authored and co-authored over 280 publications and has edited three special books on nanostructured materials and devices.

Donghwi Cho is a senior researcher of the Advanced Materials Division at the Korea Research Institute of Chemical Technology (KRICT) in Korea (2021~present). He is also the assistant professor of Advanced Materials and Chemical Engineering at the University of Science and Technology in Korea (2024~present). He received his Ph.D. degree in Materials Science and Engineering at KAIST in 2020 and started to work at Querrey Simpson Institute for Bioelectronics of Northwestern University as a postdoctoral associate (2020-2021). His research topic spans various domains, including 3D nanopatterning and material synthesis for nanostructured functional materials, and development of the advanced bioelectronic systems. He has authored and co-authored over 45 international publications.

Kwangjae Lee received his Ph.D. degree from Department of Electrical and Computer Engineering of Korea University in 2014. Now he is a professor of Department of Information Security Engineering in Sangmyung University, since 2017.

Young-Seok Shim is currently an Assistant Professor in the School of Energy, Materials & Chemical Engineering at Korea University of Technology & Education (KOREATECH), Korea since 2022. Before joining the KOREATECH, he was an Assistant Professor at Silla University (2020-2022). He received his Ph.D. (2016) degree in the Department of Materials Science & Engineering from Yonsei University, Korea. From 2016 to 2017, he was a postdoctoral research associate at the Electronic Materials Center at Korea Institute of Science & Technology (KIST). From 2018 to 2020, he joined in the Department of Materials Science & Engineering at Korea Advanced Institute of Science and Technology (KAIST) as a postdoctoral researcher. His research interests are micro/nanostructured materials and their large-area synthesis methods for gas sensing applications. He has published more than 60 international journal articles (SCI indexed).